ACS APPLIED NANO MATERIALS

www.acsanm.org Article

Polymer/Reduced Graphene Oxide/Lignosulfonate Nanocomposite Films as Pseudocapacitor Cathodes

Maricruz G. Saborio, Karen Privat, Bich Ngoc Tran, Per B. Zetterlund, Vipul Agarwal,* and Francesc Estrany*

Cite This: https://doi.org/10.1021/acsanm.1c04358 Read Online

ACCESS | Metrics & More | Article Recommendations | Supporting Information

ABSTRACT: Robust and electrochemically stable electrodes are critical for emerging energy storage devices. In this work, we describe the synthesis and characterization of an asymmetric pseudocapacitor with a P(*n*BA-*stat*-BzMA)/reduced graphene oxide (rGO, 5 wt %) nanocomposite cathode incorporating a low content of lignosulfonate (LS, 5 wt %) and a P(*n*BA-*stat*-BzMA)/rGO anode. Besides the advantageous green source and low cost of LS, its properties as a binder and its charged and redox groups contribute to the electrochemical performance improvement of the pseudocapacitor. First, the electrochemical optimization and characterization of an asymmetric unit cell is performed. Subsequently, a series of 10 unit cells are arranged in a "stack of cells"; electrochemical tests show this assembly to have a capacitance of 4.90 F cm^{-3} (8.60 F g^{-1}), maximum power of 610 W kg^{-1}, energy of 4.32 W h kg^{-1}, loss of electroactivity of 1.8%, capacitance retention of 98%, and Coulombic efficiency of 108% after 1000 charge−discharge cycles at a constant current of 0.12 A cm^{-3}. Morphological analysis revealed an increase in surface roughness after LS incorporation within the cathode. Electrode−electrolyte resistances were calculated via electrochemical impedance spectroscopy, which allowed us to propose a model of electrode−electrolyte interaction for this system.

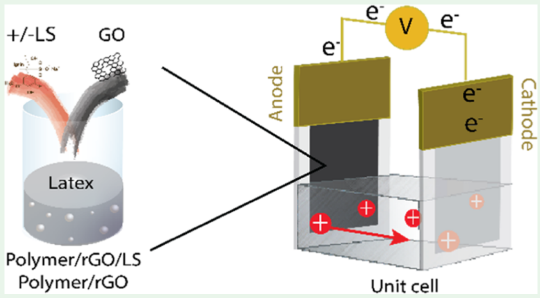

KEYWORDS: *emulsion polymerization, lignosulfonate, conductive nanocomposite electrodes, binder, pseudocapacitor, graphene, supercabatteries*

1. INTRODUCTION

The benchmark of energy storage devices (ESDs) has evolved over the years with robust and electrochemically efficient advanced materials.[1,2] The improvement of the physical and mechanical properties of ESD component materials has progressed in tandem, with the aim of producing more durable ESDs. The electrodes in ESDs undergo volumetric changes during the charge−discharge cycles due to the influx and outflow of ions from the electrolyte, resulting in the embrittlement acceleration of the electrodes. As a result, researchers have focused strongly on the mechanical integrity of electrode materials.[3]

Soft polymers have been suggested as composites with active materials (mainly carbon derivates with high conductivity) to produce flexible and stretchable materials with excellent electrical and electrochemical properties.[4,5] This elastomeric electrode component is known as a binder and is usually kept between 5 and 10 wt %.[5] The main purpose of the binder is to contain the active material and to provide structural stability. The most commonly used binders for this purpose in ESDs are fluorine-containing polymers [poly(vinylidene difluoride) (PVDF)[6] and poly(tetrafluoroethylene) (PTFE)],[7] styrene-butadiene rubber (SBR),[8] polyimides,[9] polyrotaxanes,[10] poly(acrylate) derivates,[11,12] and amphiphilic copolymers.[13]

Conducting polymer binders represent another category of binders with polyaniline (PANI),[14] polypyrrole (PPy),[15] and poly(3,4-ethylenedioxythiophene) (PEDOT)[16,17] being the most studied.[18] However, the conducting polymers have the disadvantage of the rapid deterioration of the mechanical integrity over time compared with electrodes based on elastomeric polymers.[18] Another category of binders, known as active binders, provide mechanical integrity as well as additional electrochemical performance enhancement via the improvement of adhesiveness, electrode−electrolyte interphase interaction, ion diffusion properties, and redox properties.[19] Active binders are typically ionized polymers (known as polyelectrolytes) bearing charged and/or redox-active functional groups along the main polymeric backbone. Some examples of active binders studied for different applications include poly(acrylic acid) (PAA), poly (diallyl dimethylammonium chloride) (PDDA),[20] poly(ethyleneimine) (PEI),[21] poly

Received: December 15, 2021
Accepted: February 16, 2022

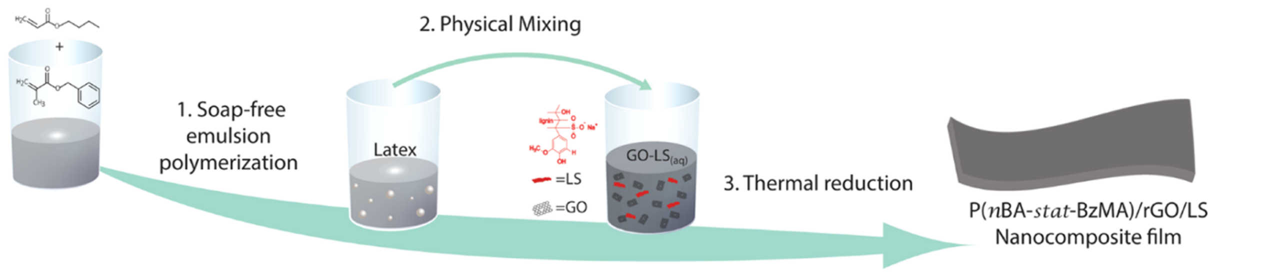

Figure 1. Schematic representation of the soap-free emulsion copolymerization reaction and the following steps for obtaining a nanocomposite film of P(*n*BA-*stat*-BzMA)/rGO/LS (represented in the figure) or P(*n*BA-*stat*-BzMA)/rGO without LS.

(allylamine hydrochloride) (PAH),[22] poly(styrene sulfonate) (PSS),[23] and "green" alternatives such as polysaccharides like carboxymethyl cellulose (CMC),[24,25] alginates,[26] and lignosulfonate (LS).[27]

LS is a versatile material which has been recently trialed as a polyelectrolyte in ESDs.[28] This polyelectrolyte compound is an amphiphilic biomacromolecule that contains a large number of ionized groups, such as sulfonate groups ($-SO_3^-$, ionized above pH = 2), carboxylate groups ($-COO^-$, ionized at pH = 3−4),[29] and pendant redox active groups like quinones.[30] The prevalence of charged groups in the LS improves ionic mobility toward the electrode via electrostatic attraction,[31] and the LS redox reactions provides extra current within the electrode.[30] This process is analogous to that which increases Li^+-ion diffusion in the binder *N*,*N*-bis(2-cyano-ethyl)-acrylamide, in which case the mechanism of ion diffusion is attributed to ionic bonding between the active binder (within the electrode) and ions in solution (from the electrolyte).[31] Similarly, electrodes incorporating LS in a composite with carbon, sulfur, and a commercial acrylonitrile multi-copolymer (LA133) binder in lithium−sulfur (Li−S) batteries have been developed, which exhibit superior capacity and life cycle retention.[32] For example, Wu and Zhong fabricated a supercapacitor electrode (LS/PANI/FGH/FCC) by anchoring a *p*-phenylenediamine-functionalized graphene hydrogel (FGH) in a functionalized carbon cloth (FCC) to load a LS/polyaniline (LS/PANI) hydrogel via the in situ polymerization of aniline in the presence of LS.[28] The symmetric supercapacitor assembled with LS/PANI/FGH/FCC electrodes and 1 M H_2SO_4 electrolyte exhibited a capacitance retention of 81% after 5000 cycles, which was interestingly lower than the FGH/FCC electrode (86% after 5000 cycles).

In addition to the nature of the electrode components mentioned, ESD optimization requires a method of synthesis that ensures homogeneous film formation with good mechanical and electrochemical properties. An optimal method will generate nanocomposite films with the lowest degree of conductive material disconnection, low electrical resistance between conductive and non-conductive domains, and better adhesion of the composite slurry to the current collector. Emulsion polymerization for synthesis of binders has been used as a method for electrode applications. For example, Qi et al.[14] used in situ two-step emulsion polymerization to synthesize poly(pyrrole/acrylonitrile-*co*-butyl acrylate) as an electrochemical double-layer capacitor electrode in which polypyrrole functioned as an electrically conducting filler for a water-based (acrylonitrile-*co*-butyl acrylate) binder. They reported a capacitance retention of ∼88.5% after 10,000 cycles (3 V window) despite the presence of only 1 wt % active material [polypyrrole relative to poly(acrylonitrile-*co*-butyl acrylate)]. To the best of our knowledge, there are no studies utilizing a three-component system (combining an inactive polymeric binder, an electroactive filler, and ionic species) to fabricate supercapacitor electrodes for ESD application.

In the present study, we aim to bridge this gap by developing a novel electrode material for ESD applications. A P(*n*BA-*stat*-BzMA)/reduced graphene oxide (rGO, 5 wt %)/LS (5 wt %) cathode and a P(*n*BA-*stat*-BzMA)/rGO nanocomposite film anode were synthesized by soap-free emulsion copolymerization based on butyl acrylate (*n*BA) and benzyl methacrylate (BzMA). Testing demonstrated the effectiveness of the nanocomposite films with LS as a cathode and without LS as an anode for the asymmetric pseudocapacitor assembly. This asymmetric pseudocapacitor configuration resulted in the improvement in current and life cycle due to cathode reinforcement with LS as a binder and its redox properties. Furthermore, the enhancement of the pseudocapacitor E and P was shown to reach commercial values through the construction of a parallel assembly of 10 unit cells in a stack of cell arrangement. A kinetic study was conducted, allowing the classification of the ESD as a pseudocapacitor. Finally, a morphological study showed that the surface area increased after binder incorporation in the cathode—a factor that contributes significantly to enhanced device performance.

2. MATERIALS AND METHODS

2.1. Materials. Monomers of *n*BA and BzMA both from Sigma-Aldrich, 99%, were purified by passing the compounds through a column of activated basic aluminum oxide (Ajax) to remove the inhibitor. The remaining materials were used as received: graphene oxide (GO, 4 mg/mL in water) from Graphenea; sodium chloride and phosphoric acid (85 w %) from Chem-Supply; and hexadecane (HD, 99%, Sigma-Aldrich), potassium persulfate (KPS, Sigma-Aldrich), sodium dodecyl sulfate (SDS, Ajax Finechem), and LS (M_w ∼ 52 kDa and M_n ∼ 7 kDa) from Sigma-Aldrich. The water used for all experiments was Milli-Q.

2.2. Electrode Synthesis of the P(*n*BA-*stat*-BzMA)/rGO/LS Cathode and the P(*n*BA-*stat*-BzMA)/rGO Nanocomposite Anode. The electrode synthesis consisted of two steps: physical mixing of polymer latex with GO dispersion and LS, in the case of the cathode, or only GO dispersion for the anode and the electrode assembly. In the following schematic, the copolymerization reaction and nanocomposite assembly are summarized (Figure 1). f1

2.2.1. Physical Mixing of Soap-Free Polymer Latex P(nBA-stat-BzMA) with Aqueous Dispersion of GO/LS for the Cathode and GO for the Anode. Nanocomposites of latex with GO and LS were prepared by soap-free emulsion copolymerization by a method similar to that described in our previous work.[1,33] The reaction incorporates *n*BA and BzMA monomer (50:50, 1.5 g) mixture and initiator KPS (0.25 M rel. to organic phase), added to water (15 mL), and mixed via magnetic stirring for 30 min. The reaction mixture was contained in a sealed glass bottle (volume 25 mL) and degassed by nitrogen bubbling for 20 min. Polymerization was conducted at 70 °C for 6 h under constant magnetic stirring and then P(*n*BA-*stat*-BzMA) was obtained. For the cathode, following polymerization, polymer latex (2 mL) was mixed with aqueous dispersion (16 mL) of SDS (1 wt %, rel. to organic phase), GO (5 wt %, rel. to monomer), and LS (5 wt %, rel. to monomer). GO was ultrasonicated earlier to this step, for 10 min, 70% power. As the last step, the dispersion was magnetically stirred for 15 min. The same procedure was followed for the anode synthesis to produce P(*n*BA-*stat*-BzMA)/rGO and with the omission of the final physical mixing step with LS.

2.2.2. P(nBA-stat-BzMA)/rGO/LS and P(nBA-stat-BzMA)/rGO Nanocomposite Electrode Assembly. Nanocomposite films were prepared by drop-casting P(*n*BA-*stat*-BzMA)/GO/LS (50 μL) onto a glass slide. The drop was spread manually into a (19 × 16 mm) rectangular shape and allowed to dry under ambient conditions for 48 h. The reduction of GO was conducted by placing the films in an air oven at 160 °C for 24 h. The same procedure was performed to produce the anode of P(*n*BA-*stat*-BzMA)/rGO.

2.3. Asymmetric Electrochemical Unit Cell Assembly. Cathode of P(*n*BA-*stat*-BzMA)/GO/LS and anode of P(*n*BA-*stat*-BzMA)/rGO were sputter-coated with 100 nm of gold (Au) (Q300T D Plus, Quorum Technologies). The Au sputter-coating was applied to the upper section of the glass slide extending 1 mm over the portion of the slide onto which the nanocomposite film was deposited. A total area of 25 × 8 mm was coated with Au to function as the current collector. Figure 2 provides a schematic

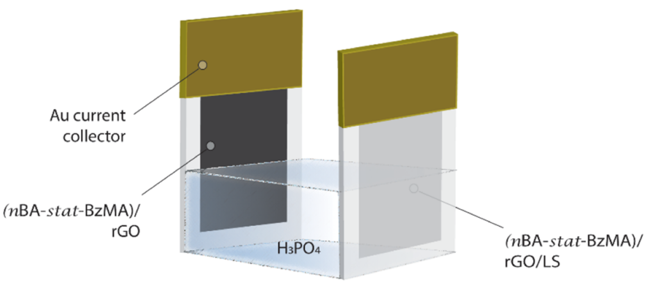

Figure 2. Schematic representation of an asymmetric electrochemical unit cell with a P(*n*BA-*stat*-BzMA)/rGO anode, a P(*n*BA-*stat*-BzMA)/rGO/LS cathode, and an electrolyte, in this case, acidic medium.

representation of an assembled cell, comprising a cathode and anode spaced 6 mm apart, with an electrolyte between the electrodes. The effective surface area of the electrode in contact with the electrolyte was fixed as 19 × 8 mm. The electrolytes used were NaCl and H_3PO_4 at concentrations of 1, 2, and 4 M each. A control symmetric cell was assembled with the cathode and anode both made of P(*n*BA-*stat*-BzMA)/rGO to allow for comparisons with the asymmetric cell and to study the effect of the addition of LS.

2.4. Stack of Cell Assembly in Acidic Electrolyte Medium. The stack of cells was built by connecting the electrodes in tandem parallel configurations. In total, 11 electrodes were produced: 6 anode and 5 cathode electrodes. Electrochemical assays were performed using 1 M H_3PO_4 as an electrolyte because under these conditions the cells returned the best values of capacitance during electrolyte optimization. For all assays, half of the electrode area was in contact with the electrolyte, avoiding false positive current values coming from the Au electrode−electrolyte interaction. The objective of the stack of cell assembly was to increase the current along with the number of cells connected in parallel and with this an increase in capacitance, *P*, and *E* values.[34]

2.5. Electrochemical Characterization. All electrochemical experiments were run in triplicate using aqueous solutions of NaCl or H_3PO_4 as electrolytes in concentrations of 1, 2 and 4 M. The assays were performed in a Biologic VMP-3 multichannel potentiostat. EC-Lab software was used to evaluate the different components of the equivalent circuit. Linear sweep voltammetry (LSV) was performed in a voltage window of −0.5 to 0.5 V and scan rate of 10 mV s^{-1}, which was defined after optimization. Cyclic voltammetry was carried out to evaluate capacitance and electrostability. Scan rates of 5, 10, 25, 50, and 100 mV s^{-1} were used in a potential window from −1 to 1 V. The values of volumetric capacitance (C_v) in F cm^{-3} (eq 1), gravimetric capacitance (C_g) in F g^{-1} (eq 2), and areal capacitance (C_a) in F/cm^2 (eq 3) were calculated by

$$C_v = \frac{1}{2v \times v}\int_{V_1}^{V_2} i \times dVo \tag{1}$$

$$C_{sp} = \frac{1}{2v \times wt}\int_{V_1}^{V_2} i \times dV \tag{2}$$

$$C_a = \frac{1}{2v \times A}\int_{V_1}^{V_2} i \times dV \tag{3}$$

where $i \times dV$ is the integral of area under the cyclic voltammetry curve, v is the scan rate in mV s^{-1}, wt is the rGO active material weight in g, A is the area in cm^2 of the nanocomposite coated, and v is the volume in cm^3 of the electrode.

Galvanostatic charge−discharge tests were run at different current rates of 0.03, 0.06, 0.12, 0.18, and 0.29 A cm^{-3}, in a potential window of 2 V. The C_v was calculated from the galvanostatic charge−discharge results as follows

$$C_v = \frac{I \times \Delta t}{(\Delta V - V_{IR}) \times v} \times 4 \tag{4}$$

where I is the current applied in A g^{-1}, Δt is the final time minus the initial time of charge in s, and ΔV is the final voltage minus the initial voltage in V. V_{IR} is current applied (I) times resistance (R) in Ω, equivalent to a voltage drop due to currents flowing through internal resistances, and v is the volume of the electrodes in cm^3. Similarly, C_g and C_a can be calculated substituting v in the denominator by an active material content within the electrodes in g or nanocomposite electrodes area in cm^2, respectively.

Another parameter calculated from the galvanostatic charge−discharge are energy (E) and power (P) density by using the following expressions

$$E = \frac{1}{2} C \times V^2 \tag{5}$$

where C is the capacitance that can be express as C_v in F cm^{-3}, C_g in F g^{-1}, C_a in F/cm^2, and V is the potential window in V, in this work (2 V − IR). The resultant E value could be expressed in W h cm^{-3}, W h g^{-1}, and W h cm^{-2} units, if C_v, C_g, and C_a were used correspondingly. Adding to this, from E, the P could be calculated

$$P = \frac{E \times 3600}{t} \tag{6}$$

where t is the time in s, E in W h cm^{-3}, W h g^{-1}, or W h cm^{-2} for obtaining the value of P in W cm^{-3}, W g^{-1}, or W cm^{-2}, respectively. The Coulombic efficiency, η_c, is another parameter to measure electrostability in ESDs. This parameter was calculated based on the galvanostatic charge−discharge assays, from the ratio between time of charge, t_c in s, and time of discharge, t_d in s, as follows

$$\eta_c = \frac{t_d}{t_c} \tag{7}$$

The capacitance retention, C_{ret}, is the variance in between the initial capacitance, Ci, and the final capacitance, Cn, and it was calculated based on the next equation

$$C_{ret} = \left(\frac{Ci}{Cn}\right) \times 100 \tag{8}$$

From the galvanostatic charge−discharge as well, the loss of electroactivity (LEA) was calculated applying the equation

$$\text{LEA}\ (\%) = \frac{\Delta C}{C_2} = \left(\frac{C_f - C_2}{C_2}\right)100 \tag{9}$$

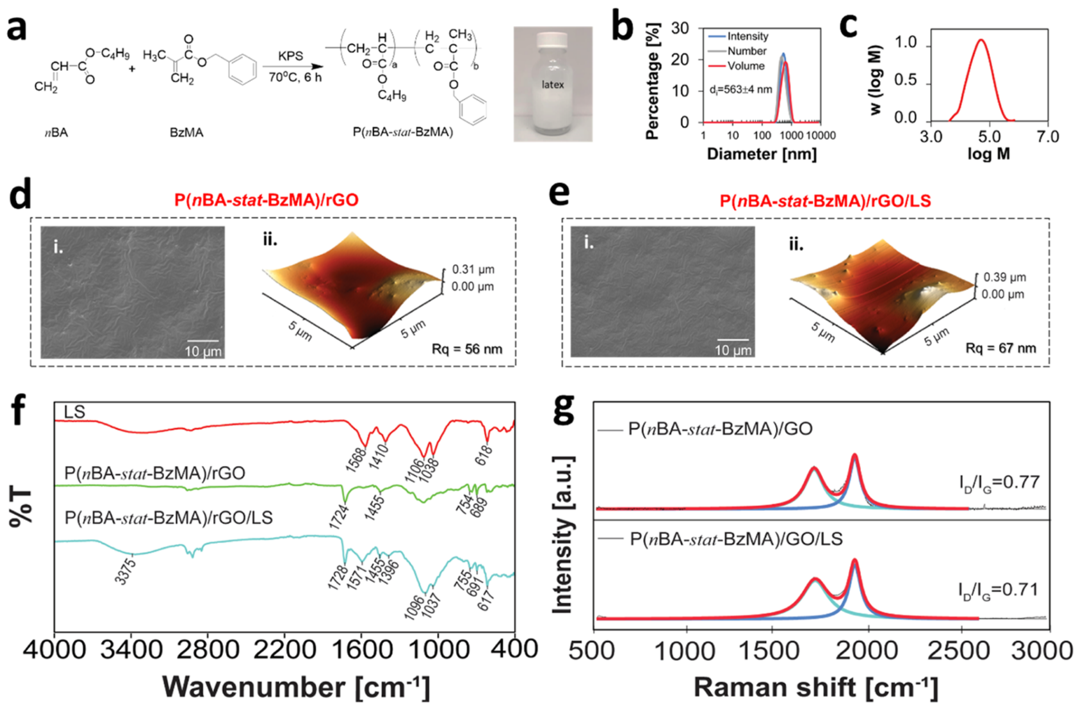

Figure 3. Schematic of the (a) chemical copolymerization reaction of latex, with a monomer conversion of 98%, and a photograph of the latex is shown; (b) plot of the polymer particle size distributions after reaction, with d_i as the intensity average diameter; (c) plot of the molecular weight distribution for *n*BA and BzMA soap-free emulsion copolymerization; (d) P(*n*BA-*stat*-BzMA)/rGO and (e) P(*n*BA-*stat*-BzMA)/rGO/LS with (i) SEM (scale bar, 10 μm) and (ii) AFM images; (f) FTIR spectra of commercial LS, P(*n*BA-*stat*-BzMA)/rGO, and P(*n*BA-*stat*-BzMA)/rGO/LS nanocomposite films; and (g) Raman spectra of P(*n*BA-*stat*-BzMA)/GO and P(*n*BA-*stat*-BzMA)/GO/LS nanocomposite films (red line represents the Lorentzian fitting).

where C_f is the last and C_2 is the second cycle of the cyclic voltammetry. Kinetic calculations were performed by plotting a logarithm of current (i) in A versus logarithm of scan rate (v) in mV s^{-1}, with i obeying a power law relation[35]

$$i = a \times v^{b} \tag{10}$$

where i is expressed in A, v in mV s^{-1}, and a and b are adjustable parameters. In the case of b, the value is the total Faradaic (diffusion-controlled) and non-Faradaic currents. When only diffusion-controlled reactions prevail in the ESD, the current will be proportional to $v^{0.5}$, then b = 0.5 (defined in Randles−Sevcik equation). Oppositely, when non-Faradaic interactions occur, a linear relationship will be stablished among the current and scan rate. Consequently, b = 1 and ESD will be more like a capacitor.

In this work, b values were obtained from the slope of logarithm of i versus logarithm of v as follows

$$\log i = b \log v + \log a \tag{11}$$

Electrochemical impedance spectroscopy measurements were conducted in a frequency range of 1 MHz to 10 mHz. The assay configuration was as follows: 25 × 8 mm Au current collector area was sputtered parallel to P(*n*BA-*stat*-BzMA)/GO/LS nanocomposite film, with 1 mm overlapped Au coated on the nanocomposite (contact area).

2.6. Morphological, Mechanical, and Topographical Characterization. Film thicknesses were obtained using an Alpha-Step D-600 stylus profiler. Prior to the measurement, the tip was calibrated using as a reference the glass surface beside the film. The film thicknesses obtained from profilometry measurements were used for electrical conductivity and (area or volume) capacitance calculations. Dynamic mechanical analysis (DMA) was performed using a TA Q800 instrument to measure the mechanical properties of the nanocomposite films. 3 mL of the latex was casted on a silicon mold and dried at room temperature before performing DMA analysis. In a typical experiment, the size of the film sample was measured with digital callipers before being placed into the calibrated tensile clamp. A torque wrench operated at a force of 3 inch-pound (in-lb) was used to fix the film into place. Measurements were conducted at a ramp force of 0.5 N/min and temperature of 25 °C. Electrodes before and after electrochemical assays were subjected to scanning electron microscopy (SEM) and atomic force microscopy (AFM) imaging by drop-casting of the P (*n*BA-*stat*-BzMA)/GO/LS dispersion (50 μL) onto a glass slide and drying under ambient temperature. Samples were sputter-coated with 10 nm platinum prior to SEM imaging. SEM images were acquired using a FEI (Thermo) Nova NanoSEM450 at 5 kV. AFM scans were acquired of 5 μm × 5 μm and 25 μm × 25 μm areas on each sample with a Bruker Dimension Icon fitted with a Scan Asyst-Air probe, operated in a manual mode with a feedback gain, peak force setpoint, and scan rate optimized for each scan. AFM data were processed using Gwyddion 2.58 software; roughness values for each scanned area were calculated following a first-order background plane fit. The AFM results show (R_q control < R_q cathode before < R_q cathode after electrochemical assays). To verify this trend over a broader area than is logistically feasible with AFM and to ensure that the results are not skewed due to anomalous, small-scale surface features/irregularities (such as precipitated salt crystals), profilometry was conducted of sample surfaces on areas from ∼70 μm × 100 μm to 1 mm × 1.42 mm, using a Keyence VK-x250 3D laser scanning microscope. Profilometry data were acquired using VK Viewer software and processed/analyzed using VK Analyzer software.

2.7. Spectroscopic and Chemical Characterization. Fourier transform infrared spectroscopy (FTIR) was executed using a Bruker Alpha II spectrometer with incorporated OPUS software. The spectra data were acquired in the wavenumber range of 400 to 4000 cm^{-1} with a resolution of 4 cm^{-1}. The presented data are the average of 32 scans. Raman spectra were acquired using a Renishaw inVia Raman microscope equipped with an Ar laser (514 nm) using a 20× objective. All Raman measurements were performed at the same laser excitation source (514.5 nm) to prevent change in the observed peak positions. The M_n for P(*n*BA-*stat*-BzMA) nanocomposite was

https://doi.org/10.1021/acsanm.1c04358
ACS Appl. Nano Mater. XXXX, XXX, XXX−XXX

determined by gel permeation chromatography (GPC) based on our previously reported method.[36−38] The polymer was dissolved in tetrahydrofuran (THF) in a ratio of 4 mg of P(*n*BA-*stat*-BzMA)/rGO/LS nanocomposite in 2 mL of THF; this solution was then centrifugated to remove rGO, LS and impurities. The GPC Agilent instrument was equipped with a Polymer laboratory 5.0 μm guard column (50 × 7.8 mm) and a four (300 × 7.8 mm) linear Phenogel columns. The eluent used was THF, at a flow rate of 1.0 mL/min, temperature of 40 °C, and an injection volume of 100 μL. The system was previously calibrated versus linear polystyrene standards 500 to 106 g/mol. Dynamic light scattering (DLS) measurements were carried out to obtain the zeta potential (mV) values of the P(*n*BA-*stat*-BzMA)/rGO/LS polymer particles; this was performed using a Malvern Zetasizer NanoSeries instrument, using a 4 mW He−Ne laser at 633 nm, 25 °C, and angle of 173°. The samples were prepared by diluting latex (~10^{-4} mg/mL) drops in Milli-Q water. The reported value is an average of three runs calculated using DTS 6.20 software.

Semi-quantitative elemental analyses of control electrodes and electrodes after electrochemical assays in 1 M H_3PO_4 and 1 M NaCl electrolytes were conducted in order to assess the presence and relative concentration of major component elements using SEM−EDS (Hitachi S−3400N SEM; Bruker X-Flash 6|30 EDS detector, Esprit 1.9 software). EDS analyses were conducted on uncoated samples at an accelerating voltage of 20 kV in the variable-pressure mode to avoid the need for the application of a conductive coating such as carbon or platinum. Quantification was done using a standardless protocol (i.e., semi-quantitative, approximate values obtained) using manually defined spectral peaks, with a ZAF matrix correction.

3. RESULTS AND DISCUSSION

3.1. Unit Cell Optimization and ESD Classification by a Kinetic Study. P(*n*BA-*stat*-BzMA) latex was synthesized using a soap-free emulsion copolymerization of *n*BA and BzMA (50:50 wt %) with KPS as an initiator (Figure 3a). The polymerization reached an overall monomer conversion of 98%. DLS analysis of the latex revealed an intensity-average particle size diameter of 563 ± 4 nm (Figure 3b) and a zeta potential −49.6 ± 0.5 mV. GPC analysis revealed a number-average molecular weight (M_n) of ~34 kg mol^{-1} (Figure 3c), which was within the typical range reported for radical polymerization under similar conditions.[1,36,39] The P(*n*BA-*stat*-BzMA) latex was subsequently combined with either just GO (5 wt % relative to the monomer) or both GO and LS (5 wt % relative to monomer) to prepare (1) P(*n*BA-*stat*-BzMA)/GO and (2) P(*n*BA-*stat*-BzMA)/GO/LS latexes. The inclusion of LS in the P(*n*BA-*stat*-BzMA) latex caused a marginal increase in the zeta potential value to −52.0 ± 0.5 mV, presumably due to the additional $-SO_3^-$ groups from LS. The high zeta potential values indicate colloidal stability of neat P(*n*BA-*stat*-BzMA) and P(*n*BA-*stat*-BzMA)/GO/LS nanocomposite latexes.

Both nanocomposite latexes were dropcasted on glass slides to enable film formation at ambient temperature. The films were thermally annealed at 160 °C for 24 h to reduce GO to electrically conduct reduced GO (rGO). SEM imaging of both thermally reduced films revealed a similar wrinkled surface morphology [Figure 3d(i),e(i)]. AFM imaging of films revealed an increase in surface roughness (R_q) from 56 nm for the P(*n*BA-*stat*-BzMA)/rGO film to 67 nm with the inclusion of LS in the nanocomposite [P(*n*BA-*stat*-BzMA)/GO/LS] [Figure 3d(ii),e(ii)]. FTIR and Raman spectroscopy were conducted to further characterize the nanocomposite films. FTIR analysis of neat LS revealed characteristic peaks at 3375, 1568, 1410, 1000−1100, and 618 cm^{-1} corresponding to an −OH stretching peak from phenolic and carboxylic acids, −C═C− stretching, −S═O stretching, −C−O stretching band from primary, secondary alcohols and aliphatic ether of LS, and −C−H vibration, respectively (Figure 3f).[40,41] In the case of the P(*n*BA-*stat*-BzMA)/rGO film, characteristic peaks for the −C═O stretching band, −C−H bending band from the methyl group, −C−O stretching vibration, and a strong −C−H band originating from a substituted benzene derivative (BzMA) were observed at 1724, 1455, 1000−1100, and 680−760 cm^{-1}, respectively (Figure 3f).[42−44] We observed the presence of peaks from both P(*n*BA-*stat*-BzMA)/rGO and LS in the P(*n*BA-*stat*-BzMA)/rGO/LS films as expected. For example, the presence of peaks, such as 1728, 1455, and ~700−760 cm^{-1}, was a contribution from P(*n*BA-*stat*-BzMA)/rGO, whereas peaks at 3375, 1571, 1396, 1000−1100, and 617 cm^{-1} can be assigned to the contribution from LS (Figure 3f). Raman analysis of the films, as shown in Figure 3g, exhibits characteristic D and G peaks of rGO at approximately ~1353 and 1586 cm^{-1}, respectively, similar to the previously published reports.[1,45] The presence of D and G peaks corresponds to the degree of structural defects in the carbon lattice and sp^2-hybridized carbon cluster in the lattice, respectively.[46] Further analysis of the D and G peaks in terms of their intensity ratios calculated from the deconvolution and Lorentzian fitting of the two peaks revealed a minor reduction in (I_D/I_G) values for P(*n*BA-*stat*-BzMA)/rGO/LS (0.71) compared to the P(*n*BA-*stat*-BzMA)/rGO film (0.77), which was in agreement with I_D/I_G values observed previously for similar thermally reduced nanocomposites.[2,38,46] The reason behind the observed marginal reduction in the I_D/I_G values with the inclusion of LS is not entirely clear. It can be postulated that LS might be interfering with the extent of reduction of GO; however, further detailed analysis is required. The reduced films were subjected to electrical conductivity measurements by LSV. We observed a significant increase in the electrical conductivity in P(*n*BA-*stat*-BzMA)/rGO/LS films (38.23 ± 0.03 S m^{-1}) compared to P(*n*BA-*stat*-BzMA)/rGO film (20.05 ± 0.01 S m^{-1}). The obtained values were in agreement with previous reports on similar nanocomposite films in terms of the composition and preparation method.[45,47] Next, nanocomposite films casted on a silicon mold were subjected to DMA to determine their mechanical properties. We observed significant reduction in mechanical behavior as adjudged by the significant systematic reduction in the strain at break with the inclusion of fillers (GO and LS) (Figure S1, Supporting Information). The P(*n*BA-*stat*-BzMA)/rGO/LS film were highly brittle with the strain at the break value (~1.4%), making it difficult to reliably accept these data. It is to be noted that all the electrochemical measurements were conducted by coating the films on glass slides to avoid the brittleness observed in standalone films.

In the present work, thermally reduced nanocomposite films were explored as a potential electrode material for ESD unit cells due to the improved electrical properties imparted by the active components such as rGO and LS in addition to the mechanical reinforcement conferred by the polymer itself. A unit cell device was prepared in an asymmetric configuration using a reduced P(*n*BA-*stat*-BzMA)/rGO/LS film coated on a glass slide as a cathode and a reduced P(*n*BA-*stat*-BzMA)/rGO film as an anode with H_3PO_4 or NaCl aqueous solution used as an electrolyte (unit cell assembly is shown in Figure 2). An asymmetric unit cell design was chosen because the presence of $-SO_3^-$ groups in the cathode from the LS lead to cation mobility enhancement from the electrolyte. The anode will

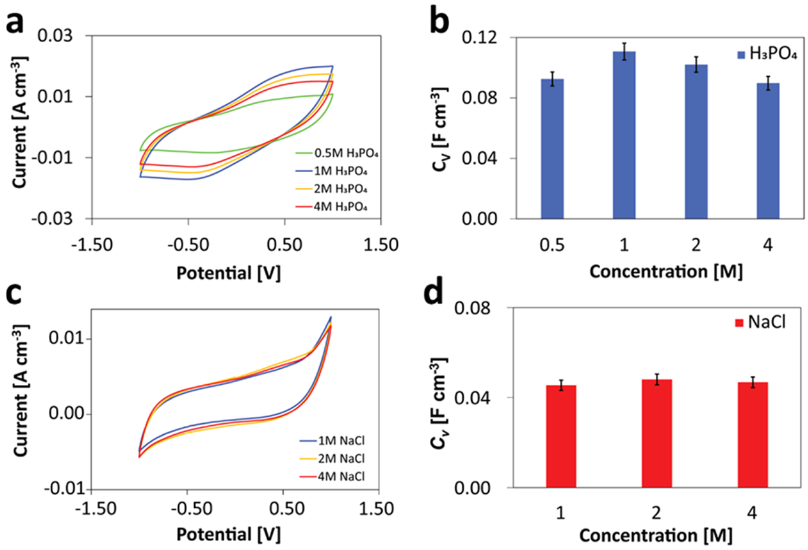

Figure 4. Plot of (a) fifth cyclic voltammetry cycle of a unit cell using 0.5, 1, 2, and 4 M H_3PO_4 as electrolytes at a scan rate of 50 mV s^{-1}; (b) C_v [F cm^{-3}] of a unit cell using 0.5, 1, 2, and 4 M H_3PO_4 as electrolytes at a scan rate of 50 mV s^{-1}; (c) fifth cyclic voltammetry cycle of a unit cell using 1, 2, and 4 M NaCl as electrolytes at a scan rate of 50 mV s^{-1}; and (d) C_v [F cm^{-3}] of a unit cell using 1, 2, and 4 M NaCl as electrolytes at a san rate of 50 mV s^{-1}.

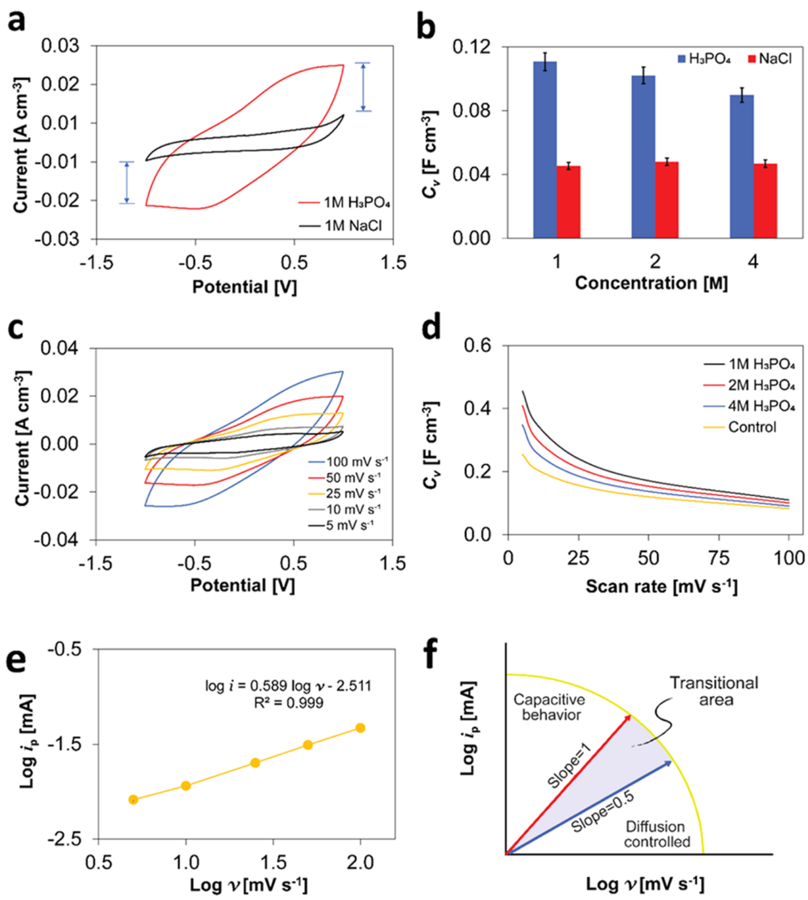

Figure 5. Plot of (a) comparison of fifth cyclic voltammetry cycle of a unit cell using 1 M H_3PO_4 and 1 M NaCl as electrolytes at a scan rate of 50 mV s^{-1}; (b) C_v [F cm^{-3}] of a unit cell using 1, 2, and 4 M H_3PO_4 and NaCl as electrolytes at a scan rate of 50 mV s^{-1}; (c) current [A cm^{-3}] at different scan rates of 5, 10, 25, 50, and 100 mV s^{-1} using 1 M H_3PO_4 as the electrolyte; (d) C_v [F cm^{-3}] comparison between a unit cell using 1, 2, and 4 M H_3PO_4 as electrolytes and a control cell using 1 M H_3PO_4 as the electrolyte, at different scan rates of 5, 10, 25, 50, and 100 mV s^{-1}; (e) log(i) vs log(ν) plot of a unit cell in the 1 M H_3PO_4 electrolyte adjusted to a linear fit; and (f) schematic representation of the log(i) vs log(ν) curve and classification of ESDs according to the slope value.

https://doi.org/10.1021/acsanm.1c04358
ACS Appl. Nano Mater. XXXX, XXX, XXX−XXX

counterbalance the cell, neutralizing the anionic species in solution. Based on these processes, an increment in capacitance is expected in comparison with symmetric cells. In addition to the current input, that pseudocapacitive redox reactions within LS in the cathode also contributed toward the overall capacitance.

The initial electrochemical optimization was divided into two stages: (1) selection of the type and concentration of the electrolyte and (2) scan rate optimization. For the first stage, the scan rate was set to an intermediate value of 50 mV s^{-1} with a fixed potential window of 2 V, for which symmetrical cyclic voltammetry plots were obtained. The electrolytes studied were $H_3PO_{4(aq)}$ at 0.5, 1, 2, and 4 M concentrations and $NaCl_{(aq)}$ at 1, 2, and 4 M concentrations. Figure 4 shows the cyclic voltammetry and calculated Cv values for both electrolytes (H_3PO_4 and NaCl) at different concentrations of a unit cell. In the case of $H_3PO_{4(aq)}$, we observed better electrochemical performance for 1 M H_3PO_4 with respect to 0.5 M H_3PO_4 (Figure 4b). The observed change can be understood by the change in the extent of ion diffusion through different layers. At 1 M H_3PO_4, ions belonging to the electrolyte will dominate the Helmholtz layer (inner layer closed to the electrode) instead of the solvent ions. The less solvent ions will result in less side reactions such as H_2 (g) generation from the water solvent resulting in a lower H_2 overpotential. Next to the Helmholtz layer is the diffusion layer, which is affected by the former phenomenon by shortening the distance required for ions to diffuse to reach the electrode.[48] In addition, the pH of the solution is another key factor improving the performance of an electrode−electrolyte combination. Previous studies claimed that a maximum ionization of sulfonate groups (present in LS in our case) would take place at pH > 2.[29] The ionized sulfonate groups will attract cations toward the cathode electrode,[31] decreasing the resistance of ion conductivity and improving the electrochemical response of the cell. In this work, the pH at 1 M H_3PO_4 was 2.6 compared to 1.6 at 0.5 M H_3PO_4 indicating that a higher ionization of sulfonate groups within LS was achieved at 1 M H_3PO_4 concentration. On the other hand, at concentrations >1 M H_3PO_4, the activity of the involved (H^+ and PO_4^{3-}) ions decreases because of the high concentration (physicochemical effect of the high ionic strength in the solution).[49] That is to say, the effective ionization of the acid is reduced at concentrations >1 M affecting the dynamic of the electrolyte solution and decreasing the capacitance. In the case of NaCl as an electrolyte, an electrochemical response was quite uniform regardless of the concentration as can be seen from the cyclic voltammetry and Cv data (Figure 4c). The reasoning behind this surprising observation is not entirely clear at this stage; however, we postulate that there could be multiple factors at play here such as (i) potential neutralization of Na^+ ions by carboxylic acid groups in LS and (ii) screening of the charged electrode due to a high number of charges at high concentrations.[50]

Figure 5a displays the cyclic voltammetry plots for the unit cell using 1 M NaCl and 1 M H_3PO_4 and illustrates the advantageous >2-fold increase in current when H_3PO_4 was used as the electrolyte. The value of the obtained current was also much higher for H_3PO_4 with respect to NaCl working at concentrations 2 M and 4 M. This may be attributed to the lower hydrated ion radius size and resultant higher ionic mobility of hydronium (H_3O^+) compared to the alkali metal ions (Na^+).[51] These mobile ions will diffuse from the electrolyte (bulk) toward the electrode and through the active material pathways within the electrode nanocomposite. In addition, the higher capacitance in H_3PO_4-based electrolytes can be attributed to its ability to ionize more free ions than the NaCl salt solution. H_3PO_4 can contribute up to three H^+ cations to the medium, while NaCl can only contribute one Na^+ cation.[52] Figure 5b summarizes the C_v of the unit cell, calculated by applying eq 1 from cyclic voltammetry measurements using different electrolyte types and concentrations; C_g and C_a values, as seen Table S1. The highest capacitance obtained for the asymmetric unit cell was 0.11 ± 0.06 F cm^{-3} at 1 M H_3PO_4 (scan rate = 50 mV s^{-1}), similar to the results obtained by Hirai et al.,[53] using acidic electrolytes. This highest capacitance at 1 M instead of 2 or 4 M concentration can be explained by the saturation of H^+ ions at the electrode surface taking place at higher H_3PO_4 electrolyte concentrations.[54] Likewise, the electrolyte viscosity increases due to ion aggregation at high concentrations delaying the ionic motion toward the electrode surface.[55] Based on the electrolyte type and concentration tests performed, 1 M H_3PO_4 was selected as the electrolyte to be used in the second stage: scan rate optimization. Figure 5c shows the cyclic voltammetry obtained for a 1 M H_3PO_4 electrolytic unit cell after applying different scan rates of 5, 10, 25, 50, and 100 mV s^{-1}. The scan rate variance did not affect the general shape of the cyclic voltammetry, disclosing good electrochemical stability and reversibility, with no perceptible extra cyclic voltammetry signatures typical of redox reactions (i.e., Faradaic reactions). However, at low scan rate (5 mV s^{-1}) extra peaks of a LS quinone redox reaction can be observed due to the longer time the ions have to diffuse and react in the electrode (see Figure S2a,b, Supporting Information).[56]

Figure 5d shows the change in the C_v value relative to a scan rate for different H_3PO_4 concentrations as an electrolyte in the unit cell and the control cell. The control cell comprised a symmetric pseudocapacitor with both the cathode and anode made of the P(*n*BA-*stat*-BzMA)/rGO nanocomposite films without LS. The figure also shows that the capacitance decreases when the scan rate increased; the highest capacitance value obtained was 0.46 F cm^{-3} for 1 M H_3PO_4 at 5 mV s^{-1}. This observed trend can be explained once again by the increase in time given for electrons and ions to diffuse and react in the electrode at low scan rates,[56] increasing the probability of having Faradaic reactions in parallel to capacitive (non-Faradaic) reactions.

At all scan rates and electrolyte concentrations, the performance of the control cell was consistently poorer in comparison to the asymmetric unit cell (containing LS in the cathode). These results indicate that the binder LS plays an important role in capacitance improvement, in addition to the optimization of the electrolyte type, concentration, and scan rate already discussed.

Further kinetic characterization based on the current change with respect to the scan rate was performed in order to accurately classify the ESD as a battery, capacitor or pseudocapacitor. The logarithm of current (i_p) versus logarithm of scan rate (ν) is plotted, as shown in Figure 5e,f. A linear relationship between the current and scan rate is obtained using eq 11, in which the slope (0.589) is a constant that correlates the highest peak of the current with respect to the scan rate obtained by cyclic voltammetry. Depending on the scan rate, different processes are favored: diffusion-controlled currents, electrochemical reactions and/or kinetic-

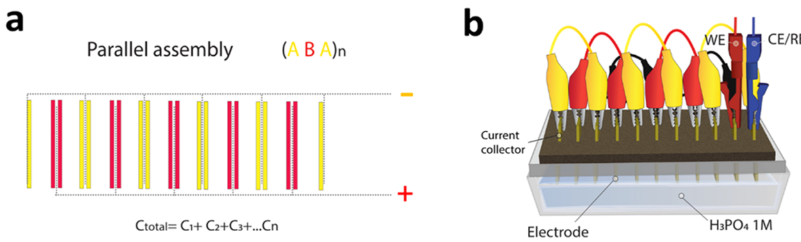

Figure 6. Schematic of the (a) parallel configuration of 10 unit cells with 9 bipolar and 2 polar electrodes (at the extremities) and (b) graphic representation of the stack of cells in the 1 M H_3PO_4 electrolyte with a total dimension of 70 × 30, 25 mm. A represents the anode (negatively charged) and B the cathode (positively charged) during the charging step, CE/RE is the counter/reference electrode, and WE is the working electrode.

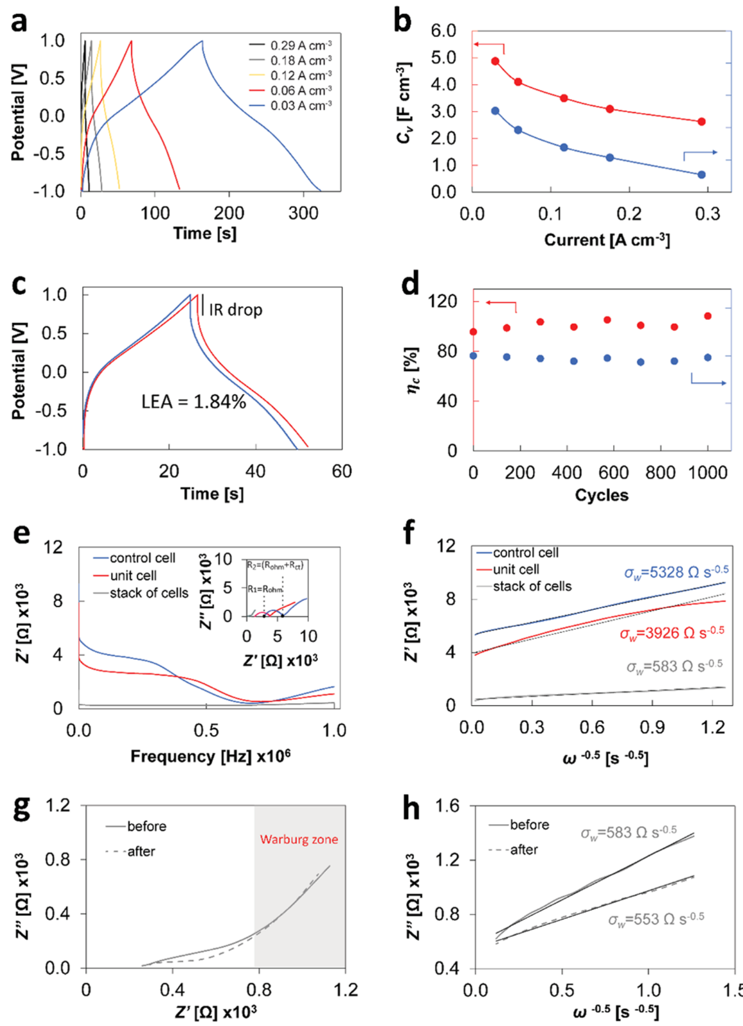

Figure 7. (a) Galvanostatic charge−discharge at different currents ranging from 0.03 to 0.29 A cm^{-3}; (b) C_v in F cm^{-3} and E in W h cm^{-3} change, with respect to current in A cm^{-3}; (c) comparison of the initial state and the final state (after 16 h, 1000 cycles) of galvanostatic charge−discharge cyclability, applying 0.12 A cm^{-3}; (d) representation of the Coulombic efficiency (η_c) and capacitance retention (C_{ret}) response after 1000 cycles; (e) Bode plot and inset of the Nyquist plot in the orthonormal scale; (f) Z' [Ω] vs $w^{-0.5}$ [$s^{-0.5}$] and diffusion coefficient values for the control cell, unit cell, and stack of cells; (g) Nyquist plot and equivalent circuit of the stack of cells [$R_1 + C_2/R_2 + W_3$], with R_1 being equal to R_{ohm}, $R_2 = (R_{ohm} + R_{ct})$ in parallel with a capacitance C_2 and a diffusive element, and W_3 the Warburg element;[17] (h) diffusion coefficient of the stack of cells, before and after 1000 cycles of galvanostatic charge−discharge.

controlled current, and capacitive electrostatic interactions. As described in Figure 5e, a slope of ≤0.5 corresponds to diffusion-controlled redox reactions typical in batteries. Meanwhile, a slope of ≥1 is driven by capacitive electrostatic interaction characteristic of electric double-layer capacitors. Figure 5f shows the kinetic analysis of the asymmetric unit cell using a 1 M H_3PO_4 electrolyte. The slope obtained was between 0.5 and 1, meaning that the device is in the "transitional" zone where the ESD is classified as a pseudocapacitor (see Figure 5e).[35] Nevertheless, the obtained slope of 0.588 was close to a value of 0.5 threshold characteristic of batteries, implying a longer time of charge

https://doi.org/10.1021/acsanm.1c04358
ACS Appl. Nano Mater. XXXX, XXX, XXX−XXX

and discharge, and E values higher than in an electrochemical capacitor (further discussed with a Ragone plot, Section 3.4). Therefore, the device developed is classified as a pseudocapacitor with capacitive (non-Faradaic) and pseudocapacitive (Faradaic) reactions taking place, for example, LS quinone reduction ranging from 1 to −1 V and vice versa (for additional details, see Figure S2a,b, Supporting Information).

3.2. Stack of Cells, Capacitance, and Electrochemical Stability. To improve the pseudocapacitor performance, different cell arrangements may be considered: an in-series connection between unit cells can be arranged to improve current or an in-parallel configuration can be assembled to expand the potential window; a combination series−parallel connection can be used if a simultaneous rise of current and potential ranges is required.[57]

In the present study a parallel arrangement of 10 unit cells was assembled (a.k.a. a stack of cells, Figure 6a,b), with a P(*n*BA-*stat*-BzMA)/rGO (functions as a non-Faradaic material) anode and a P(*n*BA-*stat*-BzMA)/rGO/LS nanocomposite film cathode (functions as a Faradaic material), immersed in a 1 M H_3PO_4 electrolyte. The tandem arrangement was proposed as a means to increase the (i) capacitive current and in turn the capacitance (due to its additive effect, $C_{total} = C_1 + C_2 + C_3 + \cdots C_n$), (ii) energy density ($E$), and (iii) power density (P) outputs. In this configuration, the stack of cells exhibits a 10-fold increase in current relative to the highest current obtained for a single cell (Figure S3b vs a, Supporting Information).[34]

The stack of cells was further characterized via a galvanostatic charge−discharge using five current settings ranging from 0.03 to 0.29 A cm^{-3} and a fixed potential window of 2 V.

Figure 7a depicts a galvanostatic charge−discharge process where a constant current is applied and the potential change with time is recorded. Initially, a charge step takes place and after a maximum potential between the working and counter electrode is reached, the discharge process starts. During this process of charge−discharge, the counter electrode will be subjected to a mirrored effect to balance charges within the electrolytic cells. The nonlinear slope during charge and discharge are characteristics of pseudocapacitive materials where reversible Faradaic reactions take place. The absence of a potential plateau in the plot indicates that there is no phase transformation of the active materials during the charge−discharge processes (an advantage over batteries).[58] Here, as indicated in the kinetic study, the capacitance is constituted of a capacitive component (non-Faradaic reactions) and pseudocapacitive component (reversible Faradaic reactions) in the electrode surface. Figure 7a also shows an inversely proportional relationship between the time of charge−discharge and the current applied; the lower the current applied, the longer the charge−discharge times and vice versa. This correlation between the time of charge and discharge and the current applied represents an opportunity to tailor the behavior of the ESD, as the current value can be adjusted to obtain a targeted time of charge and discharge in accordance with the final application requirements. Capacitance was also derived from the plot in Figure 7a by applying eq 4. These values are summarized in Figure 7b; a gradual increase of C_v was observed with a decrease in the applied current. For all capacitance calculations, the voltage drop due to insulation resistance losses (a.k.a. current−resistance drop or V_{IR} drop) were subtracted from the total 2 V window (see Figure 7c), so the uncompensated internal resistances of the stack of cells were not considered as a part of the total capacitance. The maximum capacitance observed was 4.90 F cm^{-3} within a potential window of 2 V and a current of 0.03 A cm^3. Similarly, E increased as the current applied decreased according with eq 5. The maximum capacitance value obtained for the stack of cells is high, given that the electrode is mainly a polymer with a low percentage of conductive materials (rGO = 4.63 wt % rel. to total weight). All capacitances for the stack of cells are plotted in Figure S4a,b (Supporting Information).

As a further test of electrochemical performance, galvanostatic charge−discharge cyclability was performed to assess prototype electrostability. For this analysis, a constant current of 0.12 A cm^{-3} was selected to obtain a target time of charge and discharge of approximately 50 s. The time of discharge initially obtained was 52 s, which reduced to 50 s after 16 h (1000 cycles, in a 2 V potential window) indicating a LEA of 1.8% (Figure 7c and calculated using eq 9). Also, Figure 7d depicts the Coulombic efficiency (η_c) and capacitance retention (C_{ret}) showing an average η_c value of 108% and C_{ret} = 98% after 16 h/1000 cycles of galvanostatic charge−discharge (calculated using eqs 7 and 8). The η_c value over 100% signifies that the time of charge until the cutoff potential was reached before the discharge step. This result may be attributed to the presence of remnant charges within the electrode from the former galvanostatic charge−discharge cycles accumulating and thus allowing it to reach the maximum potential more quickly. The marginal variation observed in η_c and C_{ret} can be attributed to a combination of multiple factors such as (i) slight change in the ambient temperature during measurements,[59] (ii) volume changes affecting the electrode surface roughness during the charge−discharge measurements, consequently impacting the contact area between the electrode and the electrolyte,[60] and (iii) intense polarization of the electrodes at a high applied potential (2 V) used in this work, which could affect reversibility and stability of ionic charges. The variation in η_c and C_{ret} observed in this study was similar to the trend reported previously.[61] Galvanostatic charge−discharge assays were also performed applying a lower constant current of 0.06 A cm^{-3}. Under this low current and after 62 h/1000 cycles of galvanostatic charge−discharge within a 2 V potential window, the total initial time of the charge−discharge obtained was 146 s (Figure S5, Supporting Information); LEA = 6.49%, C_{ret} = 93.5% and η_c = 100%. According to these results and the comparison of the 16 and the 62 h charge−discharge assays, it is apparent that as the applied current is reduced, the time required for E to be delivered during the discharge increases, with a consequent increase in the LEA. A C_{ret} value of 98% was higher compared to previous works. For example, Qi et al.[14] developed the most closely relatable electrode to our work made from the emulsion polymerization of pyrrole, acrylonitrile, and butyl acrylate to form poly(pyrrole/acrylonitrile-*co*-butyl acrylate), which was used as a binder to form a coin cell. They reported a C_{ret} value of 88.5% after 10,000 cycles. The reduction in specific capacitance after 10,000 cycles (yielding the C_{ret} value of 88.5%) was attributed to the presence of insulating butyl acrylate moieties in the binder matrix. To put this into context, our electrode comprises ∼90 wt % insulating component (P(*n*BA-*stat*-BzMA)) compared to ∼99 wt % in the study by Qi et al. The presence of a higher amount of the active material and combination of electronic and ionic conduction in our system compared to Qi et al. could explain the superior performance

https://doi.org/10.1021/acsanm.1c04358
ACS Appl. Nano Mater. XXXX, XXX, XXX−XXX

in terms of C_{ret} value. In another study, Wu and Zhong[28] obtained a C_{ret} value of 81% after 5000 cycles using an electrode made from the LS/PANI/functionalized graphene hydrogel/FCC using a 1 M H_2SO_4 electrolyte. Some of the other examples are presented in Table S2 (Supporting Information), where the electrochemical performance of our system is compared with other studies. It is to be noted that to the best of our knowledge, there is no study comprising a three-component system using an insulating polymer as a binder in conjunction with an electroactive component (rGO in this study) and ionic species (LS in this work); therefore, further comparison of our system was performed with two-component systems comprising a combination of an ionic and an electroactive system. As can be seen from Table S2 (Supporting Information), despite the significantly lower amount of the active material, our system exhibits a superior C_{ret} value while maintaining comparable energy and power densities compared to previous studies showcasing the advantage of our approach.

Next, electrochemical impedance spectroscopy studies were conducted to assess the electrostatic (non-Faradaic) interactions, charge/ion transfer (Faradaic) reactions, and mass transport diffusion processes in a 10 unit cell pseudocapacitor. Three different cases were evaluated: (a) control cell; cathode and anode without LS, (b) unit cell; anode without LS and cathode with LS; and (c) stack of cells; 10 unit cell duplicates arranged in parallel. The impedance assays were carried out within a frequency range of 1 MHz to 1 mHz spanning the high-, medium, and low-frequency factors. Figure 7e shows the Bode plot of resistance versus frequency for the control cell, unit cell, and stack of cells. The Ohmic resistance, R_{ohm}—which includes ionic migration, electron transport, and contact resistances—was identified for each sample as indicated on the Bode plot. The R_{ohm} obtained from the highest to the lowest followed the order: control cell > unit cell > stack of cells. As suggested in previous studies, the lower R_{ohm} for the unit cell and stack of cells compared to the control cell can be attributed to the improved adhesion between the electrode and current collector provided by the polar SO_3^- groups from the LS binder that interacts with the silanol groups of the glass slide.[3] Furthermore, in the case of the stack of cells, the bipolar electrode design is another factor that reduces the contact resistance. As shown in the Nyquist plot (inset, Figure 7e), the R_{ohm} can be identified as the value at the first "x" axis intercept of the semicircle and follows the same trend as that given by the Bode plot. As for the intermediate frequencies, the total resistance (R_{ohm} + R_{ct}) (see secondary "x" axis intercept of the semicircle) decreased from the control cell to the stack of cells. In general, the overall reduction in resistance followed the trend: control cell > unit cell > stack of cells. The decrease in resistance observed from the control cell to the unit cell to the stack of cells as reflected in the Bode plot indicates that the improved adhesion and bipolar electrodes are key factors affecting resistance. The R_{ct} drop (as visualized as the semicircle size reduction in the Nyquist plot) may be driven by the presence of LS because extra charge/ion transfer is provided through charged and redox active groups present in this biomacromolecule.[30] For example: LS in the cathode will facilitate the charge transfer of H^+ from the acidic electrolyte through the LS quinone reduction reaction (see Figure S2a,b, Supporting Information).

Another important feature in Figure 7e is the depressed shape of the semicircle, which reveals a non-Debye behavior typical in complex nanocomposites, indicating a broad relaxation time distribution of the dipoles in the nanocomposite along with the frequency change.[62] Moreover, the *knee* frequency was identified for all samples tested, that is, the frequency where the transition from capacitive to diffusive behavior takes place (inset of Figure 7e, the *knee* is located at the end of semicircle or the start of the diffusive region). Comparing the unit cell with the control cell, a higher *knee* frequency was found for the former at 845 Hz with respect to the latter at 3.4 Hz. These results reveal an outstanding improvement of ∼200-fold in the charge/ion transport as a result of the incorporation of LS within the cathode, reinforcing the higher capacitance values obtained for a single unit cell (using 1 M H_3PO_4) versus the control cell (Figure 4d).

Similarly, at very low frequencies (Hz to mHz), a complex mass transport phenomenon occurred and could be identified as an arced curve in the diffusive region (inset, Figure 7e). Huang et al.[63] claimed that this arced curve describes a complex transport process in the electrolyte, the electrode−electrolyte interphase, and within the electrode. This complex process not only considers the concentration gradient as the driving force of the diffusion phenomenon but also the migration of charged species under an electrical field.

The magnitude of the diffusion within the electrodes was quantified by plotting the resistance change versus the inverse square root of angular frequency ($\omega^{-0.5} = (2\pi f)^{-0.5}$) (Figure 7f). The plot follows the real impedance equation

$$Z' = R_{ohm} + R_{ct} + \sigma_w \omega^{-0.5} \quad (12)$$

where Z' is the real impedance, R_{ohm} and R_{ct} all of them in Ω, σ_w represents the Warburg impedance coefficient in Ω $s^{-0.5}$, and $\omega^{-0.5}$ is inverse square root of the angular frequency in $s^{-0.5}$. The slope values obtained for the control cell, unit cell, and stack of cells were σ_w: 5328, 3926, and 583 Ω $s^{-0.5}$, respectively. As the σ_w decreases, the resistance for ions to diffuse from the electrolyte to the electrode correspondingly decreases. As such, the stack of cells has better diffusion than the unit cell, and the unit cell has better diffusion that the control cell.

The higher diffusion for the pseudocapacitor incorporating LS in the cathode can be explained once again by the presence of LS functional groups ($-SO_3^-$) catalyzing the mass transport of ions from the bulk toward and within the electrode. Our outcomes are analogous to the results obtained by Yang et al.,[31] where polyelectrolyte binders in lithium−sulfur (Li−S) batteries were used to boost Li^+ mass transport.

Because the best results obtained for the stack of cells, impedance spectroscopy analyses for the stack of cells were conducted. By way of comparison, the stack of cells before and after 1000 cycles of galvanostatic charge−discharge was studied. Figure 7g depicts a Nyquist plot with a resistance−constant phase element (R/CPE) soft semicircle that drops after 1000 cycles of charge−discharge, indicating a resistance decrease of R_{ct}. The reason behind this trend could be that the electrolyte permeation improves over time aided by the hydrophilic LS groups incorporated in the electrode. Within the Warburg zone (Figure 7g), the diffusion coefficients are calculated using eq 12. Figure 7h shows the results, in which a less steep curve was observed for the stack of cells after 1000 cycles of charge−discharge. The diffusion coefficient extracted were σ_w = 553 Ω $s^{-0.5}$ after cyclability and corresponds to the same order of magnitude of the diffusion coefficient before

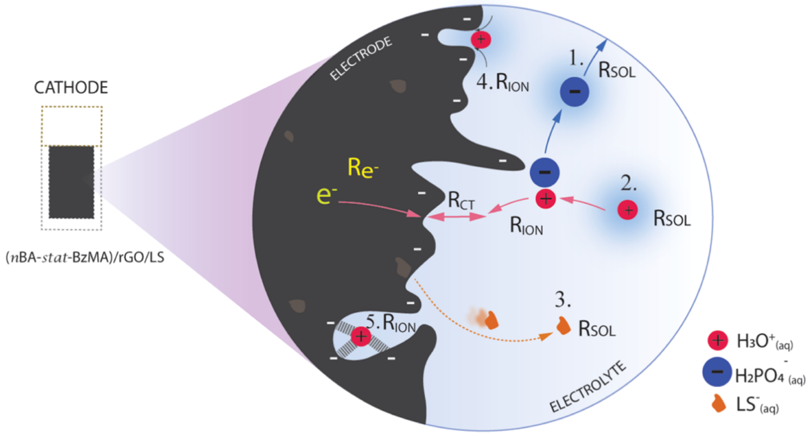

Figure 8. Schematic illustration of internal resistances at the electrode and electrolyte: (1) counterion diffusion resistance from the electrode (R_{ion}) to the electrolyte (R_{sol}), (2) ion charge-transfer resistance (R_{ct}), (3) LS diffusion resistance toward the electrolyte (R_{sol}), (4) hydrated ion size resistance to insertion within cavities (R_{ion}), and (5) resistance due to strong coordination affinity between the charged surface and the counterion (R_{ion}). The active components include $H_3O^+{}_{(aq)}$ cations and $H_2PO_4^-{}_{(aq)}$ anions resulting from the dissociation of the H_3PO_4 electrolyte in water and hydrophilic LS from the electrode.

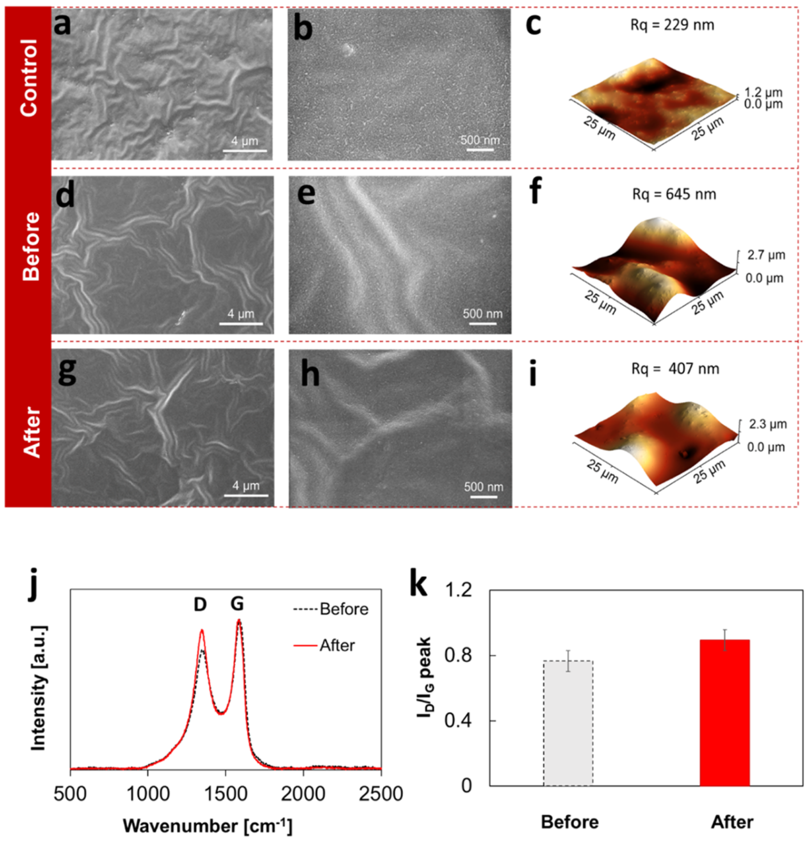

Figure 9. Surface morphology by increasing the roughness of the control electrode without LS (a–c) and the cathode with LS (d–f) prior to galvanostatic charge–discharge assays, and the cathode with LS after the galvanostatic charge–discharge assays (g–i), as shown by SEM and AFM examinations. Scale bar on SEM images is 500 nm. Representative roughness (R_q) values obtained by AFM for a (25 × 25 μm) area are given for each sample: (j) Raman spectroscopy of the cathode P(*n*BA-*stat*-BzMA)/rGO/LS nanocomposite film, before and after 1000 cycles of galvanostatic charge–discharge and (k) I_D/I_G peak ratio for the electrode before galvanostatic charge–discharge assays (control electrode) and the electrode after 1000 cycles of galvanostatic charge–discharge in the presence of 1 M H_3PO_4.

cyclability, σ_w = 583 Ω $s^{-0.5}$. This slight decrease in σ_w signifies a moderate drop in the resistance of diffusion and agrees with the excellent C_{ret} = 98% (12 h cyclability) found for the stack of cells.

Figure 8 illustrates the different resistances involved during ion mobility from the bulk to the electrode and vice versa, resistances that later will have an adverse effect in the Faradaic and non-Faradaic reactions. First, we see the role of the ion resistance to leave the cavities of the electrode (R_{ion}) and the resistance of the anion mobility toward the bulk due to solution resistance, R_{sol} (Figure 8.1). Shown also is the resistance of ions to the charge/ion transfer (R_{ct}) associated with the electronic resistance (R_e) due to electronic conduction blockage in the nanocomposite electrode material, mainly due to rGO irreversible oxidation (Figure 8.2; see also Figure 9). Other possible R_{sol} and R_{ion} sources of resistance are R_{sol} to LS dissolution in the electrolyte solution (Figure 8.3), R_{ion} to surface absorption due to the hydrated ion size being larger than the cavity size (Figure 8.4), and R_{ion} due to strong coordination that limits ion mobility (Figure 8.5).[64]

3.3. Morphological and Chemical Characterization of the Electrode Composites. To gain further insights into the morphological integrity and chemical stability of the cathode nanocomposite P(*n*BA-*stat*-BzMA)/rGO/LS before and after cyclability, the samples were subjected to SEM−energy-dispersive X-ray spectroscopy (EDS), AFM, and profilometry analyses. The cathode and anode of each case studied are shown in Table S3 and Figure S6 (Supporting Information). These techniques showed an increase in electrode roughness following LS addition to the nanocomposite formulation. One possible hypothesis to explain this increase in roughness is the segregation of the non-rubber components, such as GO and LS (referred to as hard phase) in the surroundings of polymer particles of P(*n*BA-*stat*-BzMA) (referred to as a soft phase), generating rough films after drying. In the samples studied here, we suggest LS as a part of the hard phase, located between the soft phase and aggregates when concentrated.[65] In addition, Sriring et al.[66] studied the morphology of natural rubber films in composites with non-rubber components, similar to the nanocomposite film concept used in this work. They explain that an increase in roughness can arise from the difference between the softer phase domains that will flatten out (valleys) and the harder phase that will have a positive height change (Δh) with respect to the flat domains (peaks), leading to the formation of cavities (peak−valley−peak).

The roughened film surface provides a higher surface area where active materials, such as rGO and LS, are exposed. rGO in the nanocomposite is essential for the electron transfer, and the exposed hydrophilic LS at the electrode surface for attracting ions in solution through electrostatic forces and redox reactions, contributing to the capacitance enhancement through charge/ion transfer.[30]

Figure 9 reveals that the unreacted (i.e., not subjected to any electrochemical assays) control electrode without LS has lower roughness (Figure 9c) compared to the samples containing LS as a binder before and after being subjected to electrochemical assays. The LS confers a rougher or "wrinkled" topography to the electrode (see Figure 9d,e,g,h, SEM images). This trend is also evident in the 3D AFM images (Figure 9c,f,i) from which the electrode roughness can be calculated at different scales. Over a 25 × 25 μm scan area, the roughness (R_q) values increased from the control electrode without LS, to the electrode with LS before electrochemical assays.

In the case of samples after electrochemical assays, the decrease in roughness (from R_q = 645 nm before to R_q = 407 nm after) could be explained by the volume change that the electrode undergoes due to charge−discharge cycling.[67] A constant volume change after each charge−discharge cycle is a characteristic of a dynamic process where the adsorption and desorption of ionic species takes place and could be the driving force that drags water-soluble and weakly attached compounds such as LS into the electrolytic solution (see Figure 8.3). The relative decrease of LS on the nanocomposite after charge discharge cycling relative to the control sample (before cycling) was verified by EDS (see Table S4, Supporting Information). Notwithstanding this loss, the LS in solution continued contributing to the C_{ret} via redox reactions in the electrolytic solution (Figure 7d, C_{ret} = 98%).[68]

The stability of the constituent rGO was evaluated by Raman spectroscopy. Figure 9j shows the Raman spectra for the cathode before and after charge−discharge assays. An increase in the ratio among I_D/I_G peaks after the charge−discharge assay disclose the rGO degradation through the loss of sp^2 domains and the emergence of defects (sp^3 domains). Because rGO as an active material contributes to elevated electrode conductivity, the loss of sp^2 domains signifies an increase in R_e and a decrease in conductivity, compromising the capacitance values. These results align with the 2% capacitance decrease after 1000 cycles of charge−discharge obtained before (see Figure 7d).

3.4. Stack of Cells in Ragone Plot: A Comparison. The energy and power performance of conventional capacitors, electrochemical capacitors, batteries, and the data obtained in this work are contrasted in the following Ragone plot (Figure 10).[69] Additionally, data from the two other similar studies using the emulsion polymerization for nanocomposite electrode synthesis were added to this plot for further comparison.

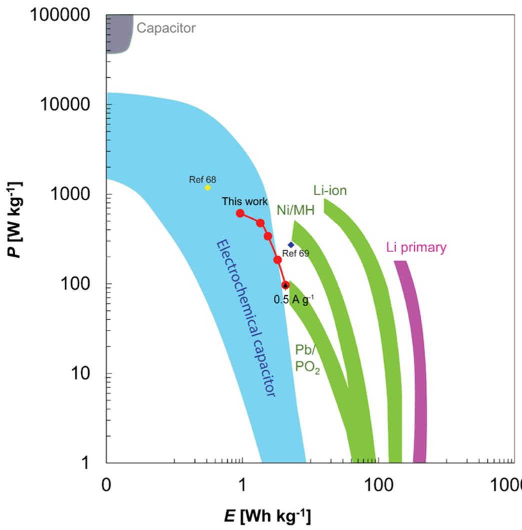

Figure 10. Ragone plot with E [W h kg^{-1}] and P [W kg^{-1}] with (1) rGO/PANI,[70] (2) rGO/poly(DVB)HIPEs,[71] and (3) stack of cells using the P(*n*BA-*stat*-BzMA)/rGO/LS cathode and the P(*n*BA-*stat*-BzMA)/rGO anode (this work) in the range of currents of 0.05 to 0.5 A g^{-1}. All the above nanocomposites used the emulsion polymerization method and rGO to obtain the final electrode nanocomposite. Reprinted from ref 69. Copyright (2022), with permission from Elsevier.

At present, an asymmetric pseudocapacitor device was developed, which bridges electrochemical capacitor and lead battery values, mainly due to a wide operating potential of 2 V. The developed device shows a wide spectrum of E and P in which it can operate and can be tuned by means of adjusting the current applied during the galvanostatic charge−discharge assays. It has been shown that, as the current increases, the P increases, and the system exhibits behavior more like an electrochemical capacitor. In contrast, as the current decreases, the E value increases, and the device behaves more like a battery. For instance, when 0.5 A g^{-1} is applied it is possible to obtain values of E and P that overlap with those of rechargeable lead batteries (PbO_2/Pb) (as depicted in Figure 10). The modular feature of the prototype developed in this study is seen as a potential to generate ESDs known as supercabatteries, with E values ranging within 10^4−10^6 W kg^{-1} and P values between 0.5×10^1 and 10^2 W h kg^{-1}.[72] The observed increase in E and P values in our study can be explained by the combination of (i) the first electrode [P(*n*BA-*stat*-BzMA)/rGO], which contributes to the overall capacitance by electrostatic interactions among the electrical double-layer capacitor generated due to the electrode polarization causing an increase in the power density. Polarization is a characteristic of carbon allotropes such as rGO, and (ii) a second electrode [P(*n*BA-*stat*-BzMA)/rGO/LS] contributes to the capacitance by electrostatic interactions due to the rGO content and Faradaic reactions (redox reactions), resulting in an increased energy density (by broadening the voltage window), which is attributed to active polymers, such as LS, used in this work.

4. CONCLUSIONS

We have demonstrated the successful synthesis and use of nanocomposite electrode materials synthesized using emulsion polymerization and physical mixing with high electrical conductivity, improved surface area, and chemical and electrochemical stability for asymmetric pseudocapacitor applications. First, we assembled a unit cell with a P(*n*BA-*stat*-BzMA)/rGO/LS cathode and a P(*n*BA-*stat*-BzMA)/rGO anode using liquid electrolytes (NaCl and H_3PO_4). Following the meticulous optimization of the unit cell, we found that higher capacitances could be achieved using a 1 M H_3PO_4 electrolyte coupled with low scan rates. Using the optimized unit cell, we prepared an asymmetric pseudocapacitor comprising 10 unit cells connected in a parallel configuration (stack of cells), which showed a 10-fold increase in capacitance with respect to the unit cell up to C_v = 4.90 F cm^{-3} as well as P_{max} = 610 W kg^{-1} and E_{max} = 4.32 W h kg^{-1}. We also obtained the C_{ret} and η_c values of 98 and 108%, respectively, after 1000 charge−discharge cycles. This study highlights the potential of emulsion-based approaches to fabricate multicomponent highly effective coatings to function as supercapacitor binders for the development of energy storage devices due to three main advantages—(i) significantly high capacitance retention (98%) despite the presence of ∼90% insulating polymer; (ii) can be easily coated on potentially any substrate; and (iii) a facile nanocomposite synthesis strategy.

■ ASSOCIATED CONTENT

Supporting Information

The Supporting Information is available free of charge at https://pubs.acs.org/doi/10.1021/acsanm.1c04358.

Electrochemical measurement of an asymmetric unit cell; cyclic voltammetry data comparing a single unit versus stack cells; galvanostatic charge−discharge cyclability data; literature comparison of pseudocapacitor performance; SEM, AFM, and profilometry analyses of two anodes in the absence and presence of electrolytes; EDS analysis of electrodes after electrochemical assays; cathode roughness profile; and electrode thickness profile before and after electrochemical assays (PDF)

■ AUTHOR INFORMATION

Corresponding Authors

Vipul Agarwal − *Cluster for Advanced Macromolecular Design (CAMD), School of Chemical Engineering, University of New South Wales, Sydney, New South Wales 2052, Australia;* orcid.org/0000-0002-6239-5410; Email: agarwalvipul84@gmail.com

Francesc Estrany − *Barcelona Research Centre in Multiscale Science and Engineering, and Department d'Enginyeria Química, Escola d'Enginyeria de Barcelona Est (EEBE), Universitat Politècnica de Catalunya, Barcelona 08019, Spain;* orcid.org/0000-0002-2696-1489; Email: francesc.estrany@upc.edu

Authors

Maricruz G. Saborio − *Cluster for Advanced Macromolecular Design (CAMD), School of Chemical Engineering, University of New South Wales, Sydney, New South Wales 2052, Australia;* orcid.org/0000-0001-8103-2466

Karen Privat − *Electron Microscope Unit, Mark Wainwright Analytical Centre, University of New South Wales, Sydney, New South Wales 2052, Australia;* orcid.org/0000-0002-6311-0990

Bich Ngoc Tran − *Cluster for Advanced Macromolecular Design (CAMD), School of Chemical Engineering, University of New South Wales, Sydney, New South Wales 2052, Australia;* orcid.org/0000-0001-5028-656X

Per B. Zetterlund − *Cluster for Advanced Macromolecular Design (CAMD), School of Chemical Engineering, University of New South Wales, Sydney, New South Wales 2052, Australia;* orcid.org/0000-0003-3149-4464

Complete contact information is available at: https://pubs.acs.org/10.1021/acsanm.1c04358

Notes

The authors declare no competing financial interest.

■ ACKNOWLEDGMENTS

P.B.Z. is grateful to the Australian Research Council for a Discovery Grant (DP190100831). V.A. acknowledges the National Health and Medical Research Council (NHMRC), Australia, for an Early Career Fellowship (GNT1139060) and UNSW for the safety fellowship. M.S.G. is grateful to Dr. Yasemin Fadil (UNSW) for emulsion polymerization training, and Le Ngoc Minh Dinh (UNSW), Rabiatul Adawiah Mat Noor (UNSW), and Namrata Maslekar for technical assistance. The authors acknowledge the facilities and the scientific and technical assistance of Microscopy Australia at the Electron Microscope Unit (EMU) within the Mark Wainwright Analytical Centre (MWAC) at UNSW Sydney.

■ REFERENCES

(1) Cai, Y.; Fadil, Y.; Jasinski, F.; Thickett, S. C.; Agarwal, V.; Zetterlund, P. B. Miniemulsion polymerization using graphene oxide as surfactant: In situ grafting of polymers. *Carbon* **2019**, *149*, 445−451.

(2) Maslekar, N.; Zetterlund, P. B.; Kumar, P. V.; Agarwal, V. Mechanistic Aspects of the Functionalization of Graphene Oxide with Ethylene Diamine: Implications for Energy Storage Applications. *ACS Appl. Nano Mater.* **2021**, *4*, 3232−3240.

(3) Cholewinski, A.; Si, P.; Uceda, M.; Pope, M.; Zhao, B. Polymer Binders: Characterization and Development toward Aqueous Electrode Fabrication for Sustainability. *Polymers* **2021**, *13*, 631.

(4) Kim, J.; Kim, J. H.; Ariga, K. Redox-Active Polymers for Energy Storage Nanoarchitectonics. *Joule* **2017**, *1*, 739−768.
(5) Song, B.; Wu, F.; Zhu, Y.; Hou, Z.; Moon, K.-s.; Wong, C.-P. Effect of polymer binders on graphene-based free-standing electrodes for supercapacitors. *Electrochim. Acta* **2018**, *267*, 213−221.
(6) Yen, J.-P.; Chang, C.-C.; Lin, Y.-R.; Shen, S.-T.; Hong, J.-L. Effects of styrene-butadiene rubber/carboxymethylcellulose (SBR/CMC) and polyvinylidene difluoride (PVDF) binders on low temperature lithium ion batteries. *J. Electrochem. Soc.* **2013**, *160*, A1811.
(7) Abbas, Q.; Pajak, D.; Frąckowiak, E.; Béguin, F. Effect of binder on the performance of carbon/carbon symmetric capacitors in salt aqueous electrolyte. *Electrochim. Acta* **2014**, *140*, 132−138.
(8) Buqa, H.; Holzapfel, M.; Krumeich, F.; Veit, C.; Novák, P. Study of styrene butadiene rubber and sodium methyl cellulose as binder for negative electrodes in lithium-ion batteries. *J. Power Sources* **2006**, *161*, 617−622.
(9) Hong, M.; Lee, S.; Choi, S.; Mun, J. Polyimide binder for a high-energy-density composite anode electrode with graphite and silicon. *J. Electroanal. Chem.* **2020**, *871*, 114317.
(10) Choi, S.; Kwon, T.-w.; Coskun, A.; Choi, J. W. Highly elastic binders integrating polyrotaxanes for silicon microparticle anodes in lithium ion batteries. *Science* **2017**, *357*, 279−283.
(11) Morooka, Y.; Nakamura, M.; Takahashi, K.; Shindo, H.; Matsuo, T. Binder for Electrodes, Electrode Material, Electrode, and Electricity Storage Device. WO 2018181772 A1, 2018.
(12) Qi, Y.; Nguyen, M. H. T.; Oh, E.-S. Effect of conductive polypyrrole in poly (acrylonitrile-co-butyl acrylate) water−based binder on the performance of electrochemical double-layer capacitors. *J. Solid State Electrochem.* **2021**, *25*, 963−972.
(13) Daigle, J.-C.; Barray, F.; Gagnon, C.; Clément, D.; Hovington, P.; Demers, H.; Guerfi, A.; Zaghib, K. Amphiphilic latex as a water-based binder for LiFePO4 cathode. *J. Power Sources* **2019**, *415*, 172−178.
(14) Male, U.; Shin, B. K.; Huh, D. S. Synthesis and characterization of polyaniline-grafted CNT as electrode materials for supercapacitors. *Macromol. Res.* **2017**, *25*, 1121−1128.
(15) Ham, H. T.; Choi, Y. S.; Jeong, N.; Chung, I. J. Singlewall carbon nanotubes covered with polypyrrole nanoparticles by the miniemulsion polymerization. *Polymer* **2005**, *46*, 6308−6315.
(16) Saborío, M. G.; Bertran, O.; Lanzalaco, S.; Häring, M.; Franco, L.; Puiggalí, J.; Díaz, D. D.; Estrany, F.; Alemán, C. Isomeric cationic ionenes as n-dopant agents of poly (3, 4-ethylenedioxythiophene) for in situ gelation. *Soft Matter* **2018**, *14*, 6374−6385.
(17) Saborío, M. C. G.; Lanzalaco, S.; Fabregat, G.; Puiggalí, J.; Estrany, F.; Alemán, C. Flexible electrodes for supercapacitors based on the supramolecular assembly of biohydrogel and conducting polymer. *J. Phys. Chem. C* **2018**, *122*, 1078−1090.
(18) Lee, S.; Gendensuren, B.; Kim, B.; Jeon, S.; Cho, Y.-H.; Kim, T.; Oh, E.-S. Effect of emulsified polymer binders on the performance of activated carbon electrochemical double-layer capacitors. *Korean J. Chem. Eng.* **2019**, *36*, 1940−1947.
(19) Zou, F.; Manthiram, A. A Review of the Design of Advanced Binders for High-Performance Batteries. *Adv. Energy Mater.* **2020**, *10*, 2002508.
(20) Lemarié, Q.; Idrissi, H.; Maire, E.; Thivel, P.-X.; Alloin, F.; Roué, L. Impact of the binder nature on the morphological change of sulfur electrodes upon cycling investigated by in situ characterization methods. *J. Power Sources* **2020**, *477*, 228374.
(21) Bae, J.; Cha, S.-H.; Park, J. A new polymeric binder for silicon-carbon nanotube composites in lithium ion battery. *Macromol. Res.* **2013**, *21*, 826−831.
(22) Shi, Y.; Ma, D.; Wang, W.; Zhang, L.; Xu, X. A supramolecular self-assembly hydrogel binder enables enhanced cycling of SnO 2-based anode for high-performance lithium-ion batteries. *J. Mater. Sci.* **2017**, *52*, 3545−3555.
(23) Cheng, M.; Liu, Y.; Guo, X.; Wu, Z.; Chen, Y.; Li, J.; Li, L.; Zhong, B. A novel binder-sulfonated polystyrene for the sulfur cathode of Li-S batteries. *Ionics* **2017**, *23*, 2251−2258.
(24) Pérez-Madrigal, M. M.; Edo, M. G.; Saborío, M. G.; Estrany, F.; Alemán, C. Pastes and hydrogels from carboxymethyl cellulose sodium salt as supporting electrolyte of solid electrochemical supercapacitors. *Carbohydr. Polym.* **2018**, *200*, 456−467.
(25) Saborío, M. G.; Svelic, P.; Casanovas, J.; Ruano, G.; Pérez-Madrigal, M. M.; Franco, L.; Torras, J.; Estrany, F.; Alemán, C. Hydrogels for flexible and compressible free standing cellulose supercapacitors. *Eur. Polym. J.* **2019**, *118*, 347−357.
(26) Ding, Y.; Zhong, X.; Yuan, C.; Duan, L.; Zhang, L.; Wang, Z.; Wang, C.; Shi, F. Sodium Alginate Binders for Bivalency Aqueous Batteries. *ACS Appl. Mater. Interfaces* **2021**, *13*, 20681−20688.
(27) Schlemmer, W.; Selinger, J.; Hobisch, M. A.; Spirk, S. Polysaccharides for sustainable energy storage−A review. *Carbohydr. Polym.* **2021**, *265*, 118063.
(28) Wu, D.; Zhong, W. A new strategy for anchoring a functionalized graphene hydrogel in a carbon cloth network to support a lignosulfonate/polyaniline hydrogel as an integrated electrode for flexible high areal-capacitance supercapacitors. *J. Mater. Chem. A* **2019**, *7*, 5819−5830.
(29) Ruwoldt, J. Critical Review of the Physicochemical Properties of Lignosulfonates: Chemical Structure and Behavior in Aqueous Solution, at Surfaces and Interfaces. *Surfaces* **2020**, *3*, 622−648.
(30) Li, F.; Wang, X.; Sun, R. A metal-free and flexible supercapacitor based on redox-active lignosulfonate functionalized graphene hydrogels. *J. Mater. Chem. A* **2017**, *5*, 20643−20650.
(31) Yang, Z.; Li, R.; Deng, Z. Polyelectrolyte binder for sulfur cathode to improve the cycle performance and discharge property of lithium−sulfur battery. *ACS Appl. Mater. Interfaces* **2018**, *10*, 13519−13527.
(32) Jeon, J.; Yoo, J.-K.; Yim, S.; Jeon, K.; Lee, G. H.; Yun, J. H.; Kim, D. K.; Jung, Y. S. Natural-wood-derived lignosulfonate ionomer as multifunctional binder for high-performance lithium−sulfur battery. *ACS Sustainable Chem. Eng.* **2019**, *7*, 17580−17586.
(33) Fadil, Y.; Dinh, L. N. M.; Yap, M. O. Y.; Kuchel, R. P.; Yao, Y.; Omura, T.; Aregueta-Robles, U. A.; Song, N.; Huang, S.; Jasinski, F.; Thickett, S. C.; Minami, H.; Agarwal, V.; Zetterlund, P. B. Ambient-temperature waterborne polymer/rGO nanocomposite films: effect of rGO distribution on electrical conductivity. *ACS Appl. Mater. Interfaces* **2019**, *11*, 48450−48458.
(34) Chiam, S. L.; Lim, H. N.; Hafiz, S. M.; Pandikumar, A.; Huang, N. M. Electrochemical performance of supercapacitor with stacked copper foils coated with graphene nanoplatelets. *Sci. Rep.* **2018**, *8*, 1−7.
(35) Simon, P.; Gogotsi, Y.; Dunn, B. Where do batteries end and supercapacitors begin? *Science* **2014**, *343*, 1210−1211.
(36) Maslekar, N.; Mat Noor, R. A.; Kuchel, R. P.; Yao, Y.; Zetterlund, P. B.; Agarwal, V. Synthesis of diamine functionalised graphene oxide and its application in the fabrication of electrically conducting reduced graphene oxide/polymer nanocomposite films. *Nanoscale Adv.* **2020**, *2*, 4702−4712.
(37) Dinh, L. N. M.; Ramana, L. N.; Kuchel, R. P.; Agarwal, V.; Zetterlund, P. B. Miniemulsion polymerization using carboxylated graphene quantum dots as surfactants: effects of monomer and initiator type. *Polym. Chem.* **2020**, *11*, 5790−5799.
(38) Tran, B. N.; Bhattacharyya, S.; Yao, Y.; Agarwal, V.; Zetterlund, P. B. In Situ Surfactant Effects on Polymer/Reduced Graphene Oxide Nanocomposite Films: Implications for Coating and Biomedical Applications. *ACS Appl. Nano Mater.* **2021**, *4*, 12461−12471.
(39) Agarwal, V.; Fadil, Y.; Wan, A.; Maslekar, N.; Tran, B. N.; Mat Noor, R. A.; Bhattacharyya, S.; Biazik, J.; Lim, S.; Zetterlund, P. B. Influence of Anionic Surfactants on the Fundamental Properties of Polymer/Reduced Graphene Oxide Nanocomposite Films. *ACS Appl. Mater. Interfaces* **2021**, *13*, 18338−18347.
(40) Ramana, L. N.; Dinh, L. N. M.; Agarwal, V. Influence of surface charge of graphene quantum dots on their uptake and clearance in melanoma cells. *Nanoscale Adv.* **2021**, *3*, 3513−3521.
(41) Agarwal, V.; McLean, D.; Horne, J.; Richardson, D.; Stack, K. Chemometric study of graft copolymerization of guar-g-(acrylamide-

co-diallyl dimethylammonium chloride). *J. Appl. Polym. Sci.* **2013**, *127*, 3970−3979.

(42) Ramana, L. N.; Agarwal, V. Nanodiamonds synthesis using sustainable concentrated solar thermal energy: applications in bioimaging and phototherapy. *Nanotechnology* **2021**, *32*, 475602.

(43) Fang, C.; Zhou, F.; Zhu, X. The application research of benzyl methacrylate (BzMA) in acrylate latex pressure sensitive adhesives. *Int. J. Adhes. Adhes.* **2021**, *107*, 102861.

(44) Samantaray, P. K.; Indrakumar, S.; Chatterjee, K.; Agarwal, V.; Bose, S. 'Template-free'hierarchical MoS 2 foam as a sustainable 'green'scavenger of heavy metals and bacteria in point of use water purification. *Nanoscale Adv.* **2020**, *2*, 2824−2834.

(45) Tran, B. N.; Thickett, S. C.; Agarwal, V.; Zetterlund, P. B. Influence of Polymer Matrix on Polymer/Graphene Oxide Nanocomposite Intrinsic Properties. *ACS Appl. Polym. Mater.* **2021**, *3*, 5145−5154.

(46) Agarwal, V.; Zetterlund, P. B. Strategies for reduction of graphene oxide − A comprehensive review. *Chem. Eng. J.* **2021**, *405*, 127018.

(47) Fadil, Y.; Thickett, S. C.; Agarwal, V.; Zetterlund, P. B. Synthesis of Graphene-based Polymeric Nanocomposites using Emulsion Techniques. *Prog. Polym. Sci.* **2022**, *125*, 101476.

(48) Pavlov, D. Lead−Carbon Electrodes. In *Lead-Acid Batteries: Science and Technology*, 2nd ed.; Pavlov, D., Ed.; Elsevier: Amsterdam, 2017; Chapter 15, pp 621−662.

(49) Pletcher, D. A. *First Course in Electrode Processes*; Royal Society of Chemistry: 2019; p 60.

(50) Romero, V.; Vázquez, M. I.; Benavente, J. Study of ionic and diffusive transport through a regenerated cellulose nanoporous membrane. *J. Membr. Sci.* **2013**, *433*, 152−159.

(51) Pal, B.; Yang, S.; Ramesh, S.; Thangadurai, V.; Jose, R. Electrolyte selection for supercapacitive devices: A critical review. *Nanoscale Adv.* **2019**, *1*, 3807−3835.

(52) Zhu, J.; Xu, Y.; Wang, J.; Lin, J.; Sun, X.; Mao, S. The effect of various electrolyte cations on electrochemical performance of polypyrrole/RGO based supercapacitors. *Phys. Chem. Chem. Phys.* **2015**, *17*, 28666−28673.

(53) Hirai, N.; Kubo, S.; Magara, K. Combined cyclic voltammetry and in situ electrochemical atomic force microscopy on lead electrode in sulfuric acid solution with or without lignosulfonate. *J. Power Sources* **2009**, *191*, 97−102.

(54) Liu, H.-h.; Zhang, H.-l.; Xu, H.-b.; Lou, T.-p.; Sui, Z.-t.; Zhang, Y. Influence of the concentration of electrolyte on the capacitive properties of vanadium nitride electrode for electrochemical capacitors. *J. Electrochem. Soc.* **2018**, *165*, A97.

(55) Lawton, J.; Tiano, S.; Donnelly, D.; Flanagan, S.; Arruda, T. The effect of sulfuric acid concentration on the physical and electrochemical properties of vanadyl solutions. *Batteries* **2018**, *4*, 40.

(56) Saborío, M. G.; Zukić, Š.; Lanzalaco, S.; Casanovas, J.; Puiggalí, J.; Estrany, F.; Alemán, C. Prototyping flexible supercapacitors produced with biohydrogel. *Mater. Today Commun.* **2018**, *16*, 60−70.

(57) Kim, B. C.; Hong, J.-Y.; Wallace, G. G.; Park, H. S. Recent progress in flexible electrochemical capacitors: electrode materials, device configuration, and functions. *Adv. Energy Mater.* **2015**, *5*, 1500959.

(58) Rajagopalan, R.; Balakrishnan, A. *Innovations in Engineered Porous Materials for Energy Generation and Storage Applications*; CRC Press, 2018; p 8.

(59) Yan, J.; Yang, L.; Cui, M.; Wang, X.; Chee, K. J.; Nguyen, V. C.; Kumar, V.; Sumboja, A.; Wang, M.; Lee, P. S. Aniline Tetramer-Graphene Oxide Composites for High Performance Supercapacitors. *Adv. Energy Mater.* **2014**, *4*, 1400781.

(60) Wang, Y.; Chen, F.; Liu, Z.; Tang, Z.; Yang, Q.; Zhao, Y.; Du, S.; Chen, Q.; Zhi, C. A highly elastic and reversibly stretchable all-polymer supercapacitor. *Angew. Chem.* **2019**, *131*, 15854−15858.

(61) Chen, X.; Su, Q.; Yu, J.; Wei, M.; Guo, G.; Wang, Y. Experimental study on the degradation mechanism of LaCoO3-based symmetric supercapacitors. *RSC Adv.* **2021**, *11*, 25170−25178.

(62) Feldman, Y.; Puzenko, A.; Ryabov, Y. Non-Debye dielectric relaxation in complex materials. *Chem. Phys.* **2002**, *284*, 139−168.

(63) Siroma, Z.; Fujiwara, N.; Yamazaki, S.-i.; Asahi, M.; Nagai, T.; Ioroi, T. Multi-rail transmission-line model as an equivalent circuit for electrochemical impedance of a porous electrode. *J. Electroanal. Chem.* **2020**, *878*, 114622.

(64) Yan, C.; Xu, R.; Xiao, Y.; Ding, J. F.; Xu, L.; Li, B. Q.; Huang, J. Q. Toward critical electrode/electrolyte interfaces in rechargeable batteries. *Adv. Funct. Mater.* **2020**, *30*, 1909887.

(65) Qiu, X.; Kong, Q.; Zhou, M.; Yang, D. Aggregation behavior of sodium lignosulfonate in water solution. *J. Phys. Chem. B* **2010**, *114*, 15857−15861.

(66) Sriring, M.; Nimpaiboon, A.; Kumarn, S.; Higaki, K.; Higaki, Y.; Kojio, K.; Takahara, A.; Ho, C. C.; Sakdapipanich, J. Film formation process of natural rubber latex particles: roles of the particle size and distribution of non-rubber species on film microstructure. *Colloids Surf., A* **2020**, *592*, 124571.

(67) Saborío, M. C. G.; Estrany, F.; Alemán, C. Properties of In situ polymerized poly (3, 4-ethylenedioxythiophene)/alumina composites for energy storage applications. *J. Polym. Sci., Part B: Polym. Phys.* **2017**, *55*, 1131−1141.

(68) Huang, J.; Zhao, B.; Liu, T.; Mou, J.; Jiang, Z.; Liu, J.; Li, H.; Liu, M. Wood-Derived Materials for Advanced Electrochemical Energy Storage Devices. *Adv. Funct. Mater.* **2019**, *29*, 1902255.

(69) Li, L.; Zhang, D.; Deng, J.; Gou, Y.; Fang, J.; Cui, H.; Zhao, Y.; Cao, M. Carbon-based materials for fast charging lithium-ion batteries. *Carbon* **2021**, *183*, 721−734.

(70) Ates, M.; Yildirim, M. The synthesis of rGO/RuO 2, rGO/PANI, RuO 2/PANI and rGO/RuO 2/PANI nanocomposites and their supercapacitors. *Polym. Bull.* **2020**, *77*, 2285−2307.

(71) Woodward, R. T.; Markoulidis, F.; De Luca, F.; Anthony, D. B.; Malko, D.; McDonald, T. O.; Shaffer, M. S. P.; Bismarck, A. Carbon foams from emulsion-templated reduced graphene oxide polymer composites: electrodes for supercapacitor devices. *J. Mater. Chem. A* **2018**, *6*, 1840−1849.

(72) Majumdar, D.; Mandal, M.; Bhattacharya, S. K. Journey from supercapacitors to supercapatteries: recent advancements in electrochemical energy storage systems. *Emergent Mater.* **2020**, *3*, 347−367.

https://doi.org/10.1021/acsanm.1c04358
ACS Appl. Nano Mater. XXXX, XXX, XXX−XXX